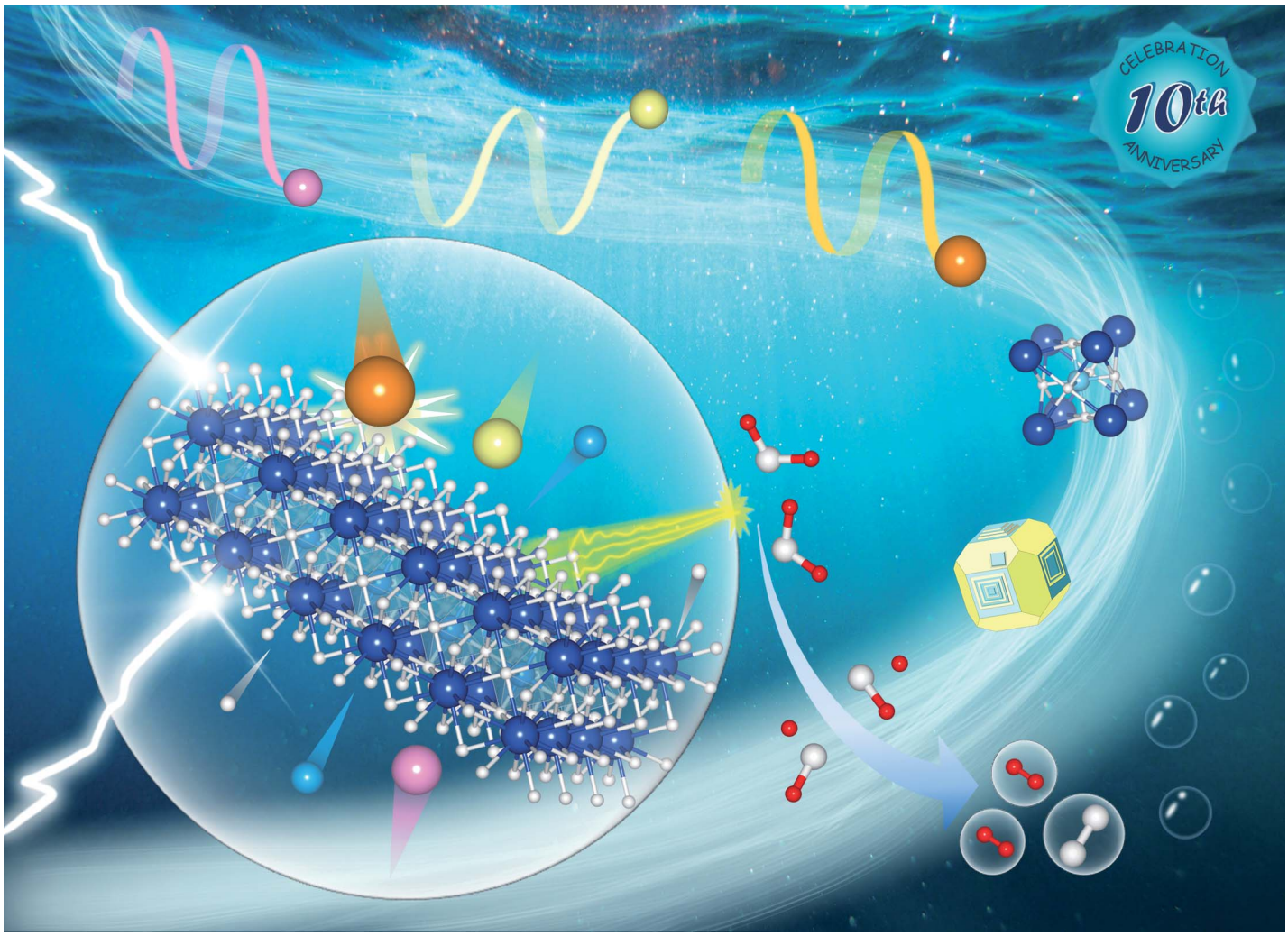

Highlighting a study on the octadecahedron $SrTiO_3$ with a nano step-shaped facet structure by CAS Key Laboratory of Green Process and Engineering, the Institute of Process Engineering, Chinese Academy of Sciences, China.

A unique octadecahedron $SrTiO_3$ perovskite oxide with a nano step-shaped facet structure for enhanced photoredox and hydrogen evolution performance

The novel octadecahedron $SrTiO_3$ has nano step-shaped facets. These facets are parallel to the (100) and (110) facets and have the characteristics of Sr-rich, O- and Ti-deficient. The crystal facet and vacancy effect improve the photocatalytic activity of $SrTiO_3$. Consequently, combined with DFT, it revealed that the effective combination of cocatalysts and the novel $SrTiO_3$ achieves higher hydrogen evolution.

As featured in:

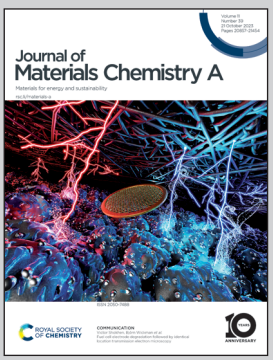

See Dongping Duan, Qibo Jia *et al.*, *J. Mater. Chem. A*, 2023, **11**, 21046.

ROYAL SOCIETY OF CHEMISTRY

rsc.li/materials-a

Registered charity number: 207890

Journal of Materials Chemistry A

ROYAL SOCIETY OF CHEMISTRY

PAPER

View Article Online
View Journal | View Issue

Cite this: J. Mater. Chem. A, 2023, 11, 21046

A unique octadecahedron $SrTiO_3$ perovskite oxide with a nano step-shaped facet structure for enhanced photoredox and hydrogen evolution performance†

Chuyu Wang,[ab] Yan Li,[b] Xiaojiao Cai,[a] Dongping Duan*[ab] and Qibo Jia*[a]

As a typical perovskite-type crystal, strontium titanate ($SrTiO_3$, STO) has remarkable photocatalytic activity and is broadly used in solar-driven overall water splitting. The research on controlling the synthesis of polyhedral STO with different exposures of crystal facets to obtain different optoelectronic properties has been greatly carried out in recent years. However, there are few reports of research on the construction of a nano step-shaped facet structure by the reconstruction of the STO crystal facet at a certain temperature, and the formation mechanism and composition analysis have not been explained clearly. In particular, the influence of crystal surface recombination on the hydrogen production reaction hasn't been thoroughly studied. This work presents the existence of a novel STO with the nano step-shaped facet structure parallel to (100) and (110) facets based on octadecahedron STO by a solid-state reaction, and the formation has been monitored by thermogravimetric analysis and *in situ* X-ray diffraction. In addition, more importantly, the step-shaped facet structure is rich in Sr, and lacks O and Ti, which is evidenced by EPR and XPS characterization, and it affects the transfer and separation of photo carriers. The complex STO catalysts were prepared by photodeposition of Rh, Cr, and Co to compare the hydrogen production capacity of overall water splitting. The novel step-shaped facet $SrTiO_3$ has a good deposition effect on the cocatalysts, and the synthesized catalyst can effectively shorten the band gap to 1.92 eV and prolong the photogenerated carriers' lifetime to 3.7356 ns. Consequently, the novel $SrTiO_3$ sample deposited co-catalysts achieve remarkable activity with the highest H_2 evolution rate of 172.0 μmol h^{-1}, which is 4.6 times higher than that of the original octadecahedron $SrTiO_3$ prepared by the hydrothermal method. The DFT calculation results prove that the excellent photocatalytic performance is due to the lower work function and effective electron transfer of the $SrTiO_3$ (100) crystal facet and Sr-rich (110) crystal facet, which is verified by the obvious electron transfer between the CrO_4^{2-} and the two kinds of crystal facets.

Received 1st June 2023
Accepted 8th August 2023

DOI: 10.1039/d3ta03239f

rsc.li/materials-a

1. Introduction

$SrTiO_3$ (STO), as a typical cubic perovskite-type semiconductor material, has strong ultraviolet (UV) absorption ability due to its band gap (3.2 eV), which endows it with high photocatalytic activity in a series of photocatalytic reactions.[1–3] However, the high recombination of photogenerated electron–hole pairs in STO limits its further application. To overcome this drawback and improve its photocatalytic performance, a variety of strategies have been employed such as building heterojunctions, hybridizing with carbon-based materials, and so on.[4,5] Nevertheless, the concept of shape-controlled morphologies is regarded as a more effective way among these strategies.

It is worth noting that a material's properties are decided not only by the chemical composition but also by the crystal size, microstructure, exposed crystal facets, *etc.* In particular, it has been proved that the photocatalytic performance of the single-crystal $SrTiO_3$ is related directly to its abundant morphologies with differently exposed crystal facets. Therefore, great efforts have been invested in the controllable preparation of $SrTiO_3$ polyhedra, hoping to strengthen its photocatalytic performance or optoelectronic efficiency. Shi and Dong *et al.*[6] synthesized

[a]CAS Key Laboratory of Green Process and Engineering, National Engineering Research Center of Green Recycling for Strategic Metal Resources, Institute of Process Engineering, Chinese Academy of Sciences, Beijing 100190, China. E-mail: douglass@ipe.ac.cn; qibojia@126.com

[b]University of Chinese Academy of Sciences, Beijing 100049, China

† Electronic supplementary information (ESI) available: Detailed information regarding the SEM graphs of hydrothermal octadecahedron $SrTiO_3$; two-dimensional diagram of the *in situ* XRD pattern; the SEM of $SrTiO_3$ after the solid-state reaction at 900 °C and 1000 °C; surface compositions and chemical state of $SrTiO_3$; the photodeposition efficiency of $SrTiO_3$; the lifetime fitting values of time-resolved fluorescence curves; the H_2 evolution over cocatalyst(s)-loaded $SrTiO_3$; the stability test of cocatalyst-loaded $SrTiO_3$. See DOI: https://doi.org/10.1039/d3ta03239f

a series of $SrTiO_3$ polyhedral micro–nano crystals from a truncated cubic structure to a truncated rhombic dodecahedral structure, which was realized by employing different alcohol compounds as facet regulators. The alcohol molecules adsorped on facets adjust the relative surface energy resulting in a gap in growth rates among crystal facets. Finally, shape-controlled $SrTiO_3$ polyhedra with the exposure of specific facets were obtained. Furthermore, Hsieh *et al.*[7] proved that the ratios of (100) and (110) crystal facets play a significant role in photocatalytic activity due to the degree of surface band bending on different $SrTiO_3$ facets. Moreover, T. Takata *et al.*[8] demonstrated that the high efficiency of hydrogen production for $SrTiO_3$ polyhedra mainly results from the exposure of crystal facets, which showed the photon utilization efficiency of aluminum-doped $SrTiO_3$ ($SrTiO_3$:Al). In our previous work, we focused on exploring the effect of $SrTiO_3$ crystal facets on the properties of photogeneration carriers.[9,10] Under the synergistic effects of exposed crystal facets and Sr–O bi-vacancy which exists on $SrTiO_3$ (110) crystal facets exclusively, self-trapping excitons with ultra-bottom binding energy and rapid formation–dissociation were generated. Compared to the common cubic $SrTiO_3$, this unique $SrTiO_3$ polyhedra produced more free carriers with longer life and better Co^{2+} photooxidation. It was found that the exposure of crystal facets presents a vital influence on the distribution of $SrTiO_3$ defects. Subsequently, we synthesized micro–nano cage $SrTiO_3$ with (110) crystal facets as a frame and hollowed out (100) crystal facets by a one-step hydrothermal method for the first time.[11,12] The multi-defect vacancies of hollow micro–nano cage $SrTiO_3$ possessed a self-trapping exciton feature and, consequently, higher efficiency for separation and longer carrier lifetime were achieved.

On the other hand, atomic defects have been considered to be the key factors affecting the electronic structure and photogenerated carrier separation at the atomic level.[13] Defect engineering provides a facile and effective approach to induce governable changes in the structure and physical properties of materials.[14,15] Calcination treatment with/without any atmosphere at varied temperatures is one of the most common approaches to constructing point defects in $SrTiO_3$ such as O-vacancies and Ti-vacancies.[16] The formation of O-vacancies leaves extra electrons behind which reduce the neighboring Ti, leading to the generation of a "homojunction of oxygen and titanium vacancies (O_V–Ti^{3+} pairs)". The charge density of semiconductors could be adjusted by high charge mobility based on the homojunction nanostructure.[17] Ye *et al.*[18] engineered rich O vacancies into $SrTiO_3$ crystals through a facile *in situ* N-doping strategy. They formed O_V–Ti^{3+} pairs with good electron transfer properties, which were energetically inclined to capture and utilize vibrationally excited oxygen species that promoted surface/interface reactions. However, to the best of our knowledge, the structure–property relationship between the crystal morphology and defect vacancies during the calcination process hasn't been studied. Furthermore, the structure–activity relationship between the carriers' characteristics related to crystal facets with morphology and vacancy, and photo-redox, particularly photolysis of water to produce hydrogen also need to be studied well.

In this work, the point defects of octadecahedron $SrTiO_3$ prepared by the hydrothermal method were constructed by calcination. Both vacancy formation and construction of a step-shaped crystal structure exist in the process of a traditional solid-state reaction, which often occurs in ceramics preparation; in particular, the re-construction of crystal planes that have completed crystallization was not emphasized and further explored due to the different professional emphasis in the field of ceramic preparation. Therefore, we focus on the recrystallization of the crystal surface and plane growth in a solid phase reaction in this study. The formation mechanism of $SrTiO_3$ with nano step-shaped crystal facets and O–Ti vacancy pairs was analyzed. The phase structure was monitored by synchronous *in situ* variable temperature XRD. The effects of vacancy and crystal facet on the photocatalytic activity were simulated by DFT. Our step-shaped octadecahedron $SrTiO_3$ performed outstandingly in photocatalytic water splitting; the hydrogen evolution rate was 4.6 times higher than that of hydrothermal octadecahedron $SrTiO_3$. Our work provides a new direction to conceive $SrTiO_3$-based polyhedral materials for applications in photocatalytic fields.

2. Experimental

2.1. Materials

Strontium chloride hexahydrate ($SrCl_2 \cdot 6H_2O$, 99.9%), titanium tetrachloride ($TiCl_4$, 99.9%), lithium hydroxide (LiOH, 99.9%), and propylene glycol ($C_3H_8O_2$, 99.9%) were purchased from Aladdin Industrial Inc. All reagents were commercial and used as received without further purification. Deionized water was used in all the experiments.

2.2. Synthesis of $SrTiO_3$

According to our previous work, octadecahedron $SrTiO_3$ (18-STO-HM) powder was prepared by a one-step hydrothermal method, and the SEM image is shown in Fig. S1a and b.† 18-STO-HM was placed in a 99-porcelain crucible and heated at 1100 °C for 10 hours to obtain the nano step-shaped facet $SrTiO_3$ (Step-STO-SSR).

2.3. Characterization

The crystal structures of the products were characterized by powder X-ray diffractometry (PXRD; X'Pert PRO MPD) using a Cu Kα radiation source. The morphologies of powders were obtained using a field-emission scanning electron microscope (ZEISS GeminiSEM 300). Transmission electron microscopy (TEM) images, high-resolution TEM (HRTEM), and energy-dispersive X-ray spectroscopy (EDS) mapping were studied on a JEOL JEM 2100F high-resolution field emission transmission electron microscope. The surface composition was investigated by X-ray photoelectron spectroscopy using an ESCALAB 250Xi and a Thermo Scientific K-Alpha. The Electron Paramagnetic Resonance (EPR) spectrum was recorded using a Bruker EMXplus-9.5/12 EPR at room temperature. Thermal stability investigations were carried out using a PerkinElmer TG-DTA6300 under an N_2 atmosphere at a heating rate of 10 °C

min^{-1}. Then, 5 mg of dried samples were loaded inside the alumina crucible, and the weight changes were monitored from 40 to 1100 °C. An Agilent Cary 5000 ultraviolet-visible diffuse reflectance spectrometer (UV-vis DRS) was employed to analyze the optical absorbance of samples. Photoluminescence (PL) spectroscopy and time-resolved fluorescence spectroscopy were carried out using an Edinburgh FLS1000 to determine the fluorescence lifetime and estimate the separation efficiency of photogenerated carriers.

2.4. *In situ* synchrotron $SrTiO_3$ study

In situ XRD experiments were carried out by using a Rigaku X-ray Diffractometer SmartLabTM 9 kW, and the sample was placed in an alumina heating table. The heating program involved heating at a constant rate of 20 °C min^{-1} from R.T. to 100 °C and remaining at that temperature for 10 min, then continuing to rise to 900 °C, with the temperature remaining constant for 10 min at every 100 °C, and finally heating to 1000 °C and 1100 °C, holding for 1 h and 2 h respectively. The recording time of diffraction patterns was set to 5 min and the 2θ angle was varied from 10° to 90°.

2.5. Photodeposition of metals and oxides

Cocatalyst composites STO-Rh/Cr_2O_3/CoOOH were synthesized by stepwise photodeposition of $RhCl_3 \cdot 3H_2O$, K_2CrO_4, and $Co(NO_3)_2 \cdot 6H_2O$. At first, $SrTiO_3$ (20 mg) was dispersed into 100 mL of distilled water, using a brief sonication. Aqueous solutions of cocatalyst precursors were prepared, with the concentration of the metal species (Rh, Cr, and Co) being 2 g L^{-1}, and the loading amount on 0.1 g STO was 0.1 wt% Rh, 0.05 wt% Cr, and 0.05 wt% Co. Using a Xe lamp (300 W, full arc) as the light source, to the reaction suspension under magnetic stirring was added the Rh aqueous solution and irradiated for 10 min. Then Cr and Co aqueous solutions were added in turns and irradiated for 5 min respectively. The mixed suspension was evaporated in an 80 °C oven until dry, followed by heating in 350 °C air for 1 h.

2.6. Photocatalytic experiments

The abilities of the photocatalyst samples were investigated in a gas-closed circulation reactor with a top irradiation lamp and an outside cooling-water jacket (to keep the reaction mixture at room temperature). Firstly, 50 mg of the photocatalyst and 20 mL of deionized water were added to the reactor to form a homogeneous suspension under stirring and then air was removed completely by vacuum. The reactor was irradiated with a 300 W Xe lamp through a quartz window. The evolved gases were analyzed with a gas chromatograph (FULI INSTRUMENT GC9790 II) equipped with a thermal conductivity detector, using Ar as a carrier gas.

2.7. DFT calculations

The optimized structure and electron density difference (EDD), and work function were calculated using Cambridge Sequential Total Energy Package (CASTEP) on Materials Studio with generalized gradient approximation in the scheme of Perdew–Burke–Ernzerhof (GGA-PBE) to describe the exchange–correlation functional. The unit cell of the cubic $SrTiO_3$ structure is relaxed with a *k*-point of $1 \times 1 \times 1$, and a cutoff energy of 571.4 eV was used for plane wave expansion. The optimized crystal parameter of $SrTiO_3$ is equal to 3.919 Å, which is in good agreement with the experimental value.[19] Based on the relaxed structure of the bulk, the slab models were cleaved to (100) and (110) directions to construct the STO (100) facet and STO (110) facet, respectively. The $(2 \times 2 \times 1)$ supercells were adopted and the vacuum layer was set to 10 Å. In the calculation of $SrTiO_3$ with chromate, the cutoff energy was set to 489.8 eV and the *k*-point was $1 \times 1 \times 1$. The convergence criteria for the SCF energy and energy gradient were set as 2×10^{-6} eV per atom and 2×10^{-5} eV per atom, respectively.

3. Results and discussion

3.1. Crystal structure

The morphology changes caused by the high-temperature solid-state reaction of 18-STO-HM are characterized by a clear nano step-shaped substructure in the (100) and (110) facets as observed from SEM in Fig. 1a–d, and the ladder appeared more frequently on the (100) crystal facet. In addition, there is a slight sintering of $SrTiO_3$ after the solid-state reaction, which is because the particles tend to have a lower surface free energy and surface area.

The detailed morphology of the Step-STO-SSR was examined by TEM images, in which the TEM imaging mode was bright-field imaging, and the details of the ladders were more directly presented. In addition, the holes observed in Fig. 1e were inside the crystal and pre-existed in 18-STO-HM (Fig. S1c and d†), which is due to the incomplete hydrothermal reaction. The calcination treatment's temperature does not reach the melting point of STO, so it does not affect the holes' structure inside the crystal. Meanwhile, TEM mapping (Fig. 1f) shows that the distribution of Sr, Ti, and O for Step-STO-SSR was roughly consistent with that of the octadecahedron STO in the previous work,[12] although the distribution of O was uneven, which is the signal deviation caused by the uneven interface due to the existence of step-shaped facets on the surface of STO. In addition, the impurity attached to STO belonged to the Ti–O compounds, which should be caused by incomplete dispersion.

The nano step-shaped facets with 13–15 nm height growing on the (100) and (110) facets were parallel to the surface orientation and the crystal surface shrinks gradually, and distinct lattice stripes can be observed with good crystallinity, as shown in Fig. 1g–j. The nano step-shaped structure resulted from surface restructuring, and it obeys the Terrace–Step–Kink (TSK) mechanism (Fig. 1k), which is frequently observed at the edges of the perovskite $BaTiO_3$ (ref. [20]) and $ZnZrO_3$ (ref. [21]) nanocrystals, and in most case, the terraces and steps lie on the (100) facet. The TSK mechanism can be explained by the periodic bond chain theory (P.B.C.), which is based on the assumption that crystal growth is due to the formation of bonds between crystalline particles (*e.g.* atoms, ions, or molecules), originally developed by Hartmann and Perdok.[22] In the P.B.C.

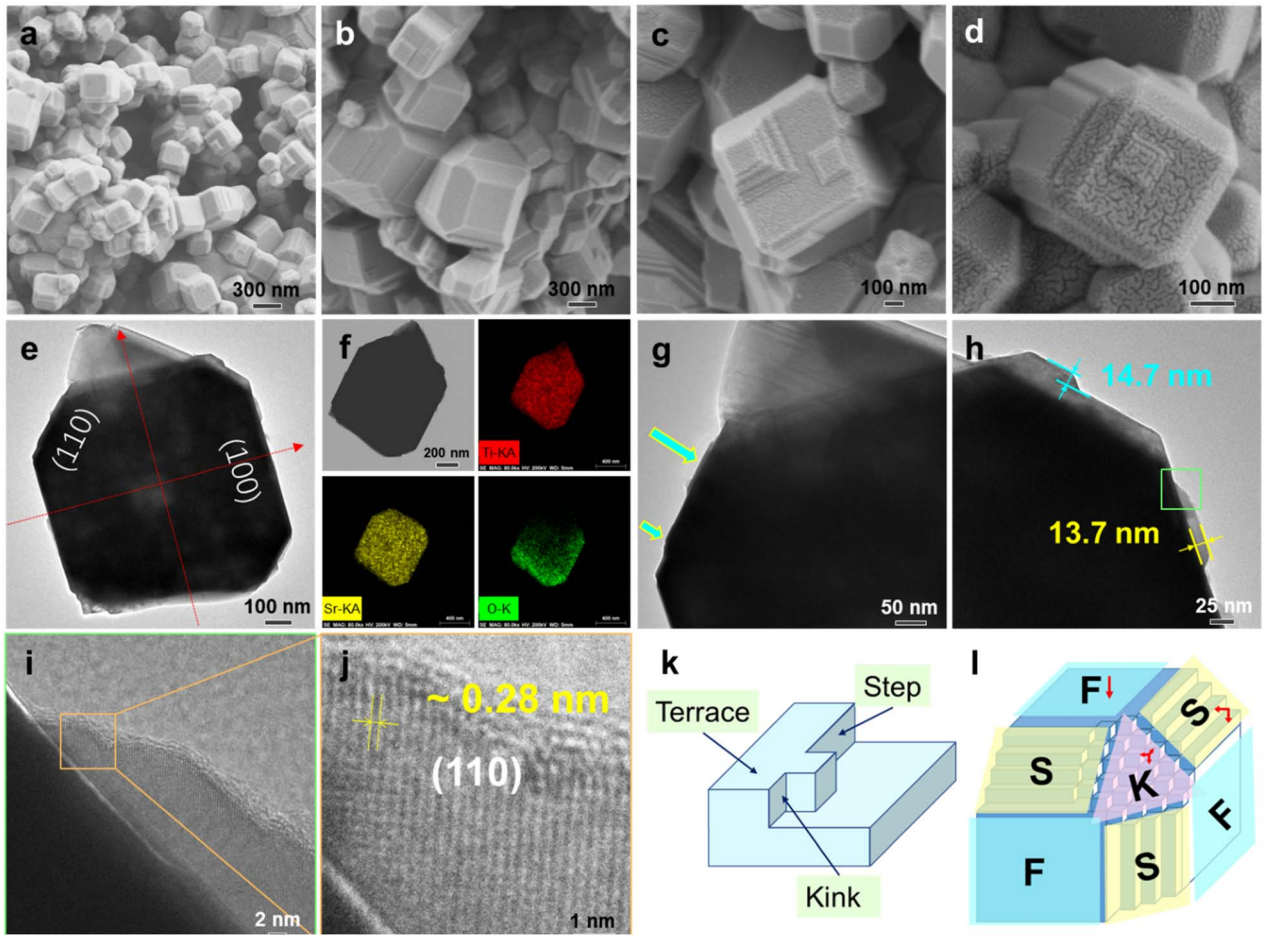

Fig. 1 (a–d) SEM graph of Step-STO-SSR. (e)The EDS elemental mappings, (f–h) TEM graph, (i and j) HR-TEM graph of Step-STO-SSR, (k) schematic diagram of the TSK structure, (l) the crystal with three P.B.C. vectors.

theory, the crystal surfaces can normally be classified into three categories, which are flat faces (F-faces, containing two or more coplanar P.B.C. vectors), stepped faces (S-faces, containing one P.B.C. vector), and kinked faces (K-faces, containing no P.B.C. vector), as shown in Fig. 1l. Therefore, the F-faces can only form one strong bond, while the S-faces can form two strong bonds and the K-faces can form three strong bonds. Hence, the displacement velocities of the F-faces are smaller than those of S-faces, and those of the K-faces are the greatest. Consequently, the F-faces ((100) facet) according to the layer mechanism with the slowest growth rate become larger faces as the final growth surface, and the K-faces ((111) facet) with the highest growth rate are often not observed or belong to the very rare forms. Occasionally, the final growth surface of the crystal would be S-faces ((110) facet). As a result, the step-shaped crystal facet is more likely to expose the F-faces and S-faces, that is, the plane of the ladder is exposed to the (100) facet, while the inclined plane is the (110) facet, which can be confirmed from the lattice fringes.

Furthermore, the inclined plane, the (110) crystal facet of the nano step-shaped structure with a lattice fringe spacing of 0.28 nm was observed in HRTEM images (Fig. 1i and j), which was larger than the standard $SrTiO_3$ facet (0.275) and closer to the anoxic $SrTiO_{2.72}$ (0.277), indicating the existence of oxygen vacancy in the nano step-shaped facet. In this case, the nano step-shaped structure arises out of the recrystallization of the crystal surface that occurs due to temperature-induced crystal surface reforming. Therefore, the instability of the crystal structure due to the strain from thermal mismatch makes Sr–O and Ti–O more prone to fracture,[23] thus oxygen spilling out of the lattice and leaving an oxygen vacancy.

3.2. Crystal surface growth mechanism and vacancy

In the process of solid-state reactions, changes in thermal effect and weight will occur along with the progress of the reaction, and this change will reflect the formation and composition changes of the nano step-shaped facet during the heating process. Therefore, TGA and DTG were combined for comprehensive thermal analysis (Fig. 2a). As is obvious from the TGA curve of $SrTiO_3$, the first weight loss occurred during heating from room temperature to 400 °C, which may be caused by the dehydration of the absorbed moisture and the decomposition of unreacted monomers and impurities in the sample. Besides, the unique weight gain occurred at around 900 °C, which was evident from the DTG curve, with the upward protruding peak

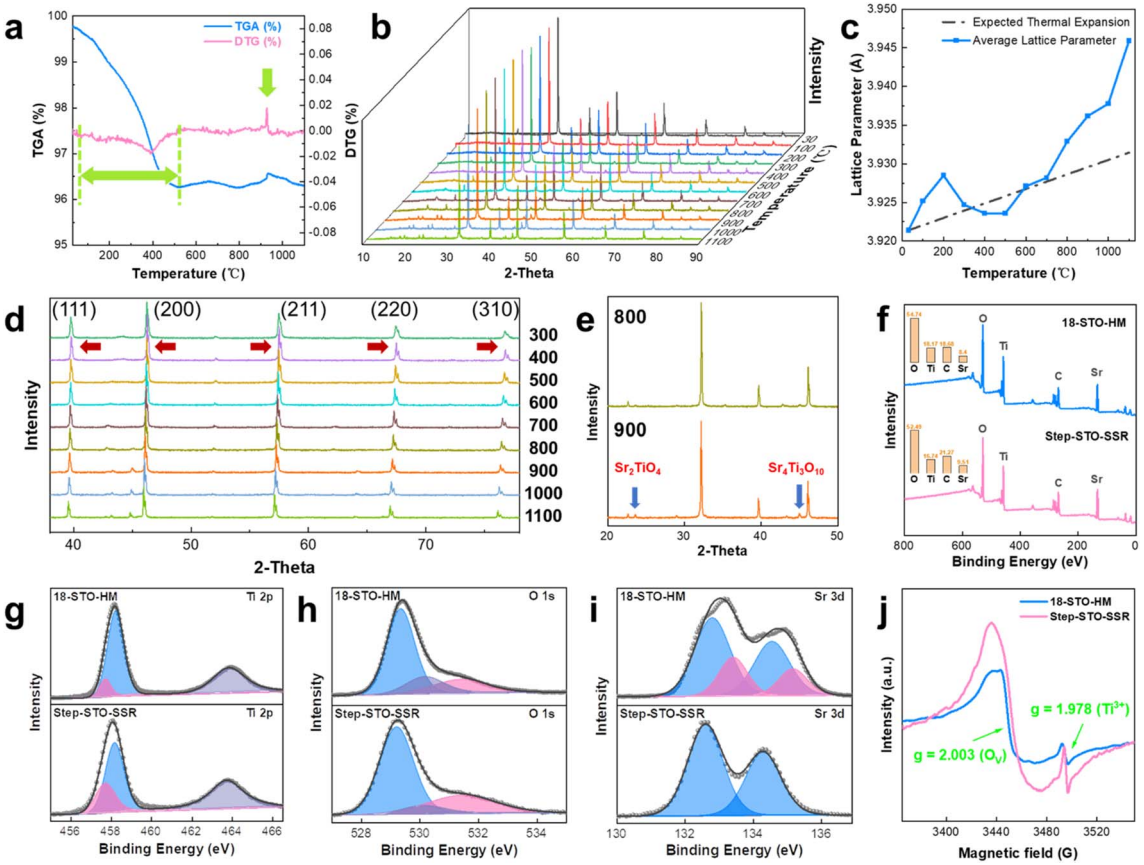

Fig. 2 (a) The TGA–DTG graph of STO. (b) Three-dimensional diagram *in situ* XRD pattern solid-state reaction of 18-STO-HM. (c) Change in the STO lattice parameter upon heating. The expected linear dependence was calculated using the coefficient of thermal expansion (9.4×10^{-6} ° C^{-1}). (d and e) The detailed graph of *in situ* XRD. (f) XPS survey spectra of STO (inset: XPS elemental relative content diagram). Ti 2p (g), O 1s (h), Sr 3d (i) XPS of STO. (j) Electron spin resonance spectra of STO.

appearing in the graph, and it is speculated to be the growth trend of the nano step-shaped crystal facet. As N_2 is passed through the whole process of the thermogravimetric test, the weight gain at 900 °C is caused by the entry of N element into the lattice during the crystal surface recombination, and the curve resumes after 1000 °C, that is, N escapes from the lattice, and in this process, the nano step-shaped crystal facet has been formed. Thus, the TGA–DTG analysis data reveal that the key temperature of step-shaped crystal facet growth is 900 °C, that is, the key temperature of crystal surface reforming.

To study crystal facet reconstruction of $SrTiO_3$ under heating conditions, *in situ* XRD was used to monitor its structural evolution with temperature, which is complementary to the TGA–DTG analysis. The three-dimensional plot of the XRD intensity as a function of the angle of incidence and temperature (30 °C to 1100 °C) is provided in Fig. 2b. At 30 °C, the XRD pattern shows peaks at 22.63°, 32.24°, 39.78°, 46.26°, 52.11°, 57.51°, 67.52°, 72.23°, 76.85°, 81.33°, and 85.79°, respectively, corresponding to (100), (110), (111), (200), (210), (211), (220), (300), (310), (311), and (222) orientations of cubic $SrTiO_3$ (Fig. S2†). In general, each diffraction peak gradually shifted to a lower angle with the increase in temperature, indicating that lattice spacing in the cell becomes larger, which is due to the strain in the lattice, and part of the change is caused by the thermal expansion of the material.[24] However, compared with the expected lattice expansion calculated from the thermal expansion coefficient (9.4×10^{-6} °C^{-1}), the lattice constant in the experiment increases more sharply, as shown in Fig. 2c.

Firstly, the lattice expansion before 200 °C is attributed to the decomposition of impurities bound to the surface, and after reaching 300 °C, the lattice constant returns to the expected value with the removal of impurities, whereas due to the existence of oxygen decomposed by the defilements, the pressure of the system increases and the lattice constant becomes smaller. Secondly, with the heating, the oxygen in the lattice will also overflow, which will lead to the formation of oxygen vacancies, causing the lattice spacing to widen again.[25] Integrating with the XRD pattern in Fig. 2d at 400 °C, the (111), (200), (211), (220), and (310) peaks began to split, which is characteristic of hypoxic STO (such as $SrTiO_{2.72}$ and $SrTiO_{2.6}$), and the split became rather obvious with the increase of temperature. In addition to the factors of oxygen vacancy and thermal expansion, the reduction of Ti will also lead to the increase of lattice parameters. In the *in situ* XRD diagram at 800 °C and 900 °C (Fig. 2e), there are small peaks belonging to $Sr_4Ti_3O_{10}$ and Sr_2TiO_4, and that proves the decrease of Ti^{4+} because part of Ti^{4+}

was reduced to Ti^{3+}. In a nitrogen atmosphere, the oxygen in the crystal is consumed continuously with the increase in temperature, and Ti^{4+} is reduced to Ti^{3+}, which is consistent with the subsequent analytical results of XPS and EPR. On account of the radius of Ti^{3+} (67 pm) ions being larger than that of Ti^{4+} (60.5 pm), lattice parameters increased. During the formation of oxygen vacancy and Ti defect, the STO crystal surface becomes Sr rich. Furthermore, by comparing the change of the XRD peak intensity, the strongest (110) peak with the most obvious change decreased significantly at 900 °C. Then the peak intensity in the XRD spectrum is related to the proportion of the exposed crystal facet, which means that the proportion of (110) facet in the total crystal facet decreases with the decline of (110) peak intensity. Combined with the analysis of the nano step-shaped facet growth, the ladder parallel to the crystal surface was more likely to appear on the (100) facet, thus reducing the specific gravity of the (110) facet. The supplementary experiment also confirmed that the crystal surface reforming started at 900 °C, and the nano step-shaped structure appeared on some of the crystal surfaces (Fig. S3a and b†). When the temperature rose to 1000 °C, the nano step-shaped facet structure appeared on most of the $SrTiO_3$ particles (Fig. S3c and d†). This supports the TGA–DTG and *in situ* XRD crystal surface recrystallization analysis.

On the other hand, the full width at half maximum of the (110) peak was estimated. Under the equal measurement conditions, the difference in the FWHM of XRD peaks emerges from the distinction in the crystallite dimension and degree of crystallinity. The FWHM of the (110) peak at 30 °C, 900 °C, 1000 °C and 1100 °C were 0.1671, 0.1574, 0.1518, and 0.1458 respectively, that is, the crystallinity of STO improved with the increase of solid-state reaction temperature. Therefore, the solid-state reaction treatment improves the crystallinity of the sample to a certain extent.

More surface properties and electronic structures can be brought about by XPS analysis. C 1s was corrected to 284.80 eV as a reference for calibrating all other peaks. The XPS spectrum of Step-STO-SSR was roughly the same as that of 18-STO-HM, but the elemental content on the surface was slightly different, as shown in Fig. 2f. In Step-STO-SSR, the content of Ti and O elements decreased while that of Sr increased, indicating that the crystal facet has more Ti defects and O vacancies, and is Sr-rich, which conformed to the above formation mechanism. The high-resolution XPS spectrum of Ti 2p for STO is displayed in Fig. 2g, and it can be deconvoluted into three peaks after the Gaussian fit, as shown in Table S1.† The two strong peaks centered around the binding energy of 458.2 eV and 463.8 eV correspond to the Ti $2p_{3/2}$ and Ti $2p_{1/2}$ of Ti^{4+}. Notably, a tiny Ti $2p_{3/2}$ peak was detected at 457.7 eV, reflecting the existence of reduced Ti^{3+} species in the material,[26] which was caused by the abundant oxygen vacancy formed after the solid-state reaction. The Ti^{3+} content of Step-STO-SSR was 19.91%, while that of 18-STO-HM was 14.47%, that is, the Step-STO-SSR contains more oxygen vacancy.

Detailed information about oxygen vacancy can be obtained from the O 1 s peak spectrum (Fig. 2h). It can be resolved into three peaks at about 529.2 eV, 530.1 eV, and 531.4 eV as shown in Table S1,† and the first two peaks can be ascribed to lattice oxygen[27] (O_{lat}), and the last peak to the oxygen vacancy[28] (O_V). The dominant peak at 529.2 eV is in agreement with O 1s electron binding energy arising from the $SrTiO_3$ lattice, while the peak at 530.1 eV is assigned to the titanium oxide lattice. The results show that the 18-STO-HM contains more titanium oxide lattice oxygen (16.9%); the presumed reason is that after the solid-state reaction, part of the titanium oxide was transformed into $SrTiO_3$ during the crystal surface recombination, therefore, Step-STO-SSR has lower titanium oxide lattice oxygen (7.2%). Furthermore, the O_V content of Step-STO-SSR (27.0%) is 1.5 times that of 18-STO-HM (18.2%), proving that $SrTiO_3$ has more oxygen vacancy due to the appearance of the step-shaped crystal facet after solid phase treatment.

In the high-resolution XPS spectrum of Sr 3d (Fig. 2i), double peaks at 132.6 eV and 134.3 eV of Step-STO-SSR can be attributed to Sr $3d_{5/2}$ and Sr $3d_{3/2}$ of $SrTiO_3$, respectively. In the case of 18-STO-HM, the two states of strontium in Sr 3d spectra, Sr $3d_{5/2}$ at 132.8 eV and 133.4 eV, were assigned to $SrTiO_3$ and $SrCO_3$ species. Therefore, the peaks belonging to $SrCO_3$ disappear after the solid-state reaction, and it leads to the inference that the $SrCO_3$ impurities in the hydrothermal reaction decomposed after the solid-state reaction, and served as the raw material for ladder formation.

Besides, the EPR spectra of the two kinds of STO showed a strong O_V signal[29] ($g = 2.003$) and a hyperfine splitting at $g = 1.978$ relevant to the Ti^{3+} signal[17] that emerged simultaneously (Fig. 2j). The difference in peak intensity demonstrated that the oxygen vacancy and Ti^{3+} species content of Step-STO-SSR were more than those of 18-STO-HM. These results suggested a considerable increase in O_V after the solid-state reaction, and the surface restructuring resulted in atomic rearrangement and triggered electronic reconstruction and local disorder around Ti, manipulating a partial reduction of Ti^{4+} to Ti^{3+}. Then, the formation of Ti^{3+} is accompanied by a considerable increase in O_V to maintain the local charge balance, resulting in the formation of O_V–Ti^{3+} pairs.[30] The accumulation of excess electrons around Ti atoms caused by oxygen vacancies was beneficial to the electron transfer caused by Ti atoms as electron donors.[18] In addition, the peak at $g = 2.003$ for Step-STO-SSR was distinctly broadened, indicating that the crystal defects lead to a longer electron relaxation time.[31] Consequently, the formation of O_V–Ti^{3+} pairs brings about an easier electron transfer behavior and enhanced the redox ability of strontium titanate. In addition, Zhu *et al.*[32] found that annealing $SrTiO_3$ at 1100 °C with $Sr_3Ti_2O_7$, that is, under the Sr-rich condition, the photoredox properties of some (110) facets can be changed from photooxidation to photoreduction, and the (110) facets become the bifunctional crystal facet. Moreover, Pisat *et al.*[33] reported that the photo-reduced behavior of the crystal surface was associated with a surface composition that had a greater Sr/Ti ratio. Based on these experimental findings, we speculate that the Sr-rich surface caused by the formation of Step-STO-SSR will also promote photoreduction performance.

A new "nano step-shaped crystal facet structure" concept, characteristics, and mechanism are proposed at the nanoscale for clarification. The nano step-shaped structure is formed by the recrystallization of the crystal surface to form new crystals

at a certain solid phase temperature, which obeys the TSK mechanism, thus resulting in the step morphology. Meanwhile, influenced by the growth rate of the crystal face, the possibility of the nano step-shaped structure appearing on the (100) crystal face is greater. Moreover, this phenomenon of crystal laddering, which is a non-atomic scale concept, is common in ceramics but has been ignored because the researchers do not focus on the growth of individual particles.[34,35] In 18-STO-HM, the electron configuration of the atoms in $SrTiO_3$ changes near 1000 °C, and leads to the local change of the chemical potential of the atom or ion, thus driving the solid-state reaction on the crystal surface. As shown in Fig. 3, adsorption of raw materials occurs on the $SrTiO_3$ crystal surface first; when the system reaches the reaction temperature, atoms at the $SrTiO_3$ interfaces react with each other to form a new $SrTiO_3$ nucleus, that is, the nucleation reaction occurs. In this process, with $SrTiO_3$ as the growth template, the rearrangement of reactants at the $SrTiO_3$ interface is relatively easy due to the structure of the crystal nucleus being similar to that of the substrate. The fracture and recombination of anion and cation bonds in the reactant structure result in the absence, diffusion, and entry of ions in the reactant lattice.[23,36] However, in this process, due to the recombination of the crystal surface, there will be redundant defect vacancies, such as oxygen vacancies, which lead to Ti^{3+} defects.

3.3. Photocatalytic capacity evaluation and theoretical calculation

To verify that the nano step-shaped facet structure and vacancy effect are related to the photocatalytic conversion properties of $SrTiO_3$, the photodeposition capacity and hydrogen production capacity of two kinds of STO were compared, to quantify the REDOX capacity of STO. Using a stepwise photodeposition method, 0.1 wt% Rh, 0.05 wt% Cr, and 0.05 wt% Co were loaded on $SrTiO_3$ to obtain the photocatalysts. During the photodeposition process, photoexcited electrons reduce the Rh ions and Cr ions to form Rh and Cr_2O_3 nanoparticles. Rh promotes both the hydrogen evolution reaction (HER) and oxygen reduction reaction (ORR). When Cr_2O_3 is deposited on Rh to form a core–shell structure, the ORR reaction occurs by preventing the generated O_2 from contacting the Rh core. Meanwhile, part of Cr_2O_3 on the surface of STO was in the form of nanoclusters, increasing the absorption of visible light and shortening the band gap, accelerating the electron transfer.[37] Additionally, photoexcited holes oxidized Co ions to form CoOOH and Co_3O_4, which promotes the oxygen evolution reaction (OER), and promotes the total water splitting kinetics.[38,39]

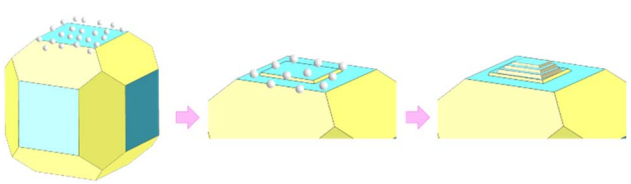

Fig. 3 Schematic diagram of the growth process of Step-STO-SSR.

The photodeposition capacities of the two kinds of STO are compared in Fig. S4.† The conversion ability of 18-STO-HM and Step-STO-SSR to Rh and Co is up to 98%, among which the former is slightly higher. However, the reduction capacity of the two kinds of STO for Cr is relatively low and the difference is large, the photodeposition efficiency of Cr of 18-STO-HM is only 35.3%, while that of Step-STO-SSR is 48.6%.

Next, to investigate the crystal phase structure and composition of the synthesized catalyst and the surface chemical composition and electronic state of cocatalysts on the surface of $SrTiO_3$, the XRD and XPS characterizations were analyzed. The XRD pattern (Fig. 4a) shows that the perovskite structure of strontium titanate is not changed by the photodeposition reaction, but the absence of metal peaks in the pattern is caused by the low content of the loaded metal. Furthermore, the XPS spectra of STO loaded with Rh, Cr_2O_3, and CoOOH are shown in Fig. 4b–d. Firstly, the peak of Rh 3d close to 309 eV is ascribed to Rh_2O_3, while that near 306 eV corresponded to Rh metal. The Rh species on 18-STO-HM was mainly in the form of Rh_2O_3, while Step-STO-SSR was loaded with Rh metal additionally. Secondly, the Cr 2p peaks at 577 eV and 587 eV belong to Cr_2O_3, while peaks at 580 eV, 583 eV, and 589 eV correspond to CrO_3, Cr metal, and K_2CrO_4, respectively. The results show that Step-STO-SSR converted most of the CrO_4^{2-} to Cr_2O_3, and a small part existed in the form of CrO_3, and in addition to CrO_x, a part of CrO_4^{2-} in 18-STO-HM was not converted, and Cr metal was present. Finally, the Co 2p peak at 780 eV belongs to CoOOH, and peaks at 786 eV belong to $Co(OH)_2$, while those at 786 eV and 795 eV are attributed to Co_3O_4. Thus, Step-STO-SSR was loaded with CoOOH and Co_3O_4, while $Co(OH)_2$ and Co_3O_4 were deposited on 18-STO-HM.

Furthermore, the influence of the cocatalysts on optical absorption and photogenerated carrier lifetime of STO was studied by ultraviolet-visible diffuse reflectance spectroscopy (UV-vis DRS) and photoluminescence (PL) emission spectra. As shown in Fig. 4e, all samples exhibit strong absorption peaks in the ultraviolet region, and the samples loaded with cocatalysts reflect improved absorption in the visible region. The band gap values are calculated from the absorption data *via* the Tauc relationship (Fig. 4f). Step-STO-SSR with the advantages of vacancies and crystal facets has a lower band gap value (E_g = 2.80 eV) than 18-STO-HM (E_g = 2.94 eV). Moreover, the loaded cocatalysts have a greater influence on the light absorption and band gap of Step-STO-SSR, which was reduced to 1.92 eV, while that of 18-STO-HM loaded with cocatalysts was reduced to 2.85 eV. Thus, it can be concluded that STO with step-shaped crystal facets and high concentration vacancies can slightly enhance the light adsorption, and its close contact with the cocatalysts will further improve the light absorption in the visible light region and reduce the band gap. Combining the photoluminescence emission signals and transient decay spectra, the photogenerated charge separation behavior and efficiency in STO loaded with cocatalysts can be described. As shown in Fig. 4g, the PL spectra for both 18-STO-HM and Step-STO-SSR loaded with cocatalysts show an emission peak of about 440 nm, and the latter has a much lower emission peak, indicating that the more photogenerated charge separation and

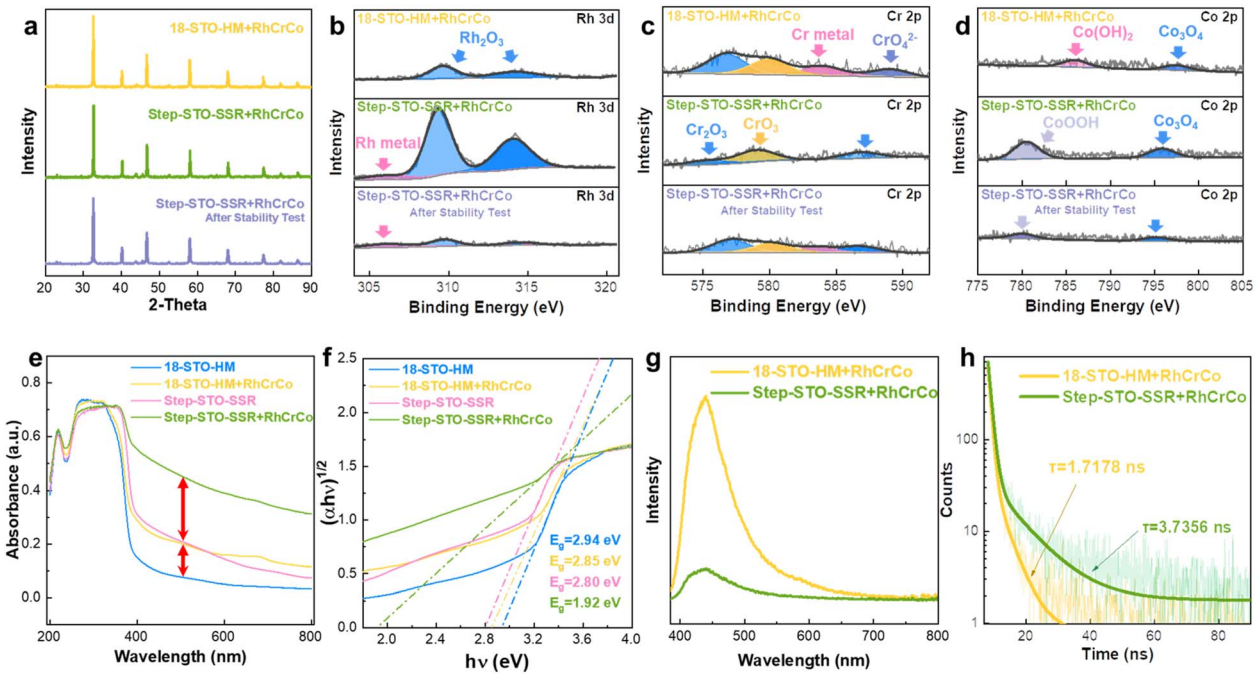

Fig. 4 The XRD pattern (a), XPS spectra (b–d), UV-vis DRS (e) and corresponding Tauc image (f), PL spectrum (g), time-resolved fluorescence spectroscopy (h) excited at 375 nm of all synthesized $SrTiO_3$ particles.

transfer occur in Step-STO-SSR loaded with cocatalysts. Then, the decay kinetics for the two STO revealed the lifetime of photogenerated carriers, and the fitting values are summarized in Table S2.† The Step-STO-SSR loaded with cocatalysts has a longer average lifetime, which was 3.7356 ns, while that of 18-STO-HM loaded with cocatalysts was only 1.7178 ns (Fig. 4h). The results imply that Step-STO-SSR which is combined more closely with the cocatalysts facilitates charge transfer and leads to reduced charge recombination. In addition, Fig. 5a–d exhibit the micro-structure of the Step-STO-SSR loaded with cocatalysts by SEM and TEM. The results showed that the morphology of step-shaped crystal facets didn't change after photodeposition, and the cocatalysts exist as nanoparticles on the surface of STO. The HR-TEM (Fig. 5e) revealed the close contact between the STO and Rh, the 0.27 nm spacing was in agreement with STO (110) crystal facet, while the lattice spacing of 0.22 nm belonged to the metal Rh (111) crystal facet, supporting the existence of Rh metal. Then, the elemental mapping analyses were captured by area scanning (Fig. 5f–l), which showed that loaded cocatalysts were uniformly distributed on the STO surface, and the step-shaped crystal facet was loaded with more cocatalysts, presenting a higher activity.

The photocatalytic properties of the two types of STO are further demonstrated by the photolysis of water to produce hydrogen. Fig. 6a and b show the H_2 production dependence on time for the two samples and the corresponding H_2 evolution

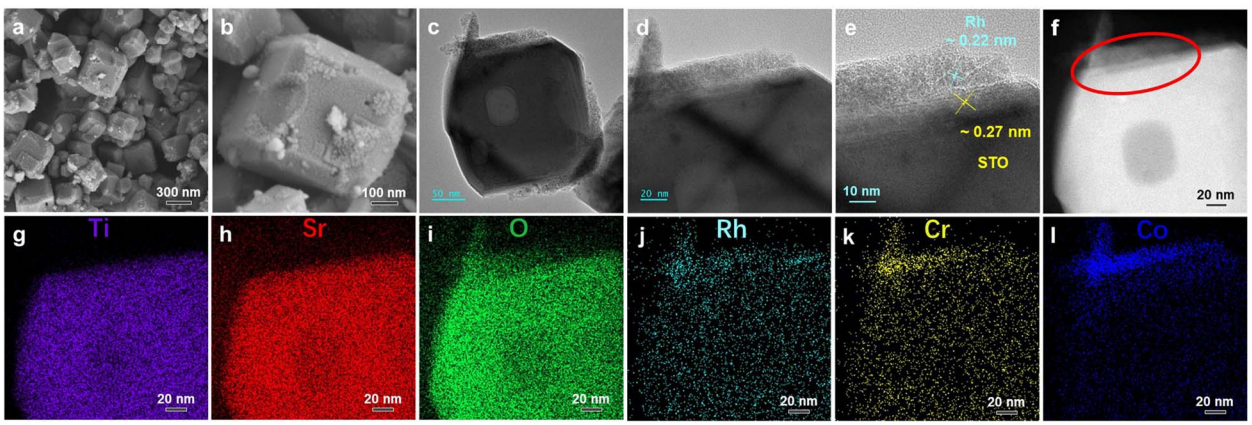

Fig. 5 The SEM graph (a and b), TEM and HR-TEM graph (c–f), and EDS elemental mappings (g–l) of the Step-STO-SSR loaded with 0.1 wt% Rh, 0.05 wt% Cr, and 0.05 wt% Co.

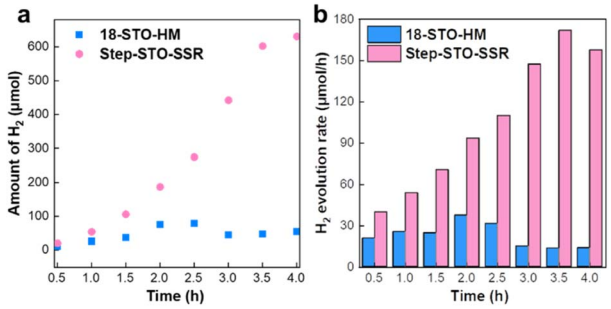

Fig. 6 (a) Photodeposition efficiency of STO. (b) H_2 production by the overall water-splitting of $SrTiO_3$ with Rh (0.1% wt%)/Cr (0.05 wt%)/Co (0.05 wt%) and (c) the corresponding H_2 evolution rates.

rates. The results show that 18-STO-HM and Step-STO-SSR give the average H_2 evolution rates of 22.70 μmol h^{-1} and 105.55 μmol h^{-1}, respectively. The H_2 evolution rates of Step-STO-SSR increased over 3.5 h, and the highest rate reached 172.0 μmol h^{-1}, while that of 18-STO-HM decreased at 2 h, and the highest rate was only 37.4 μmol h^{-1}. Furthermore, the dependence of water-splitting activities on the components of cocatalysts was studied, as shown in Fig. S5.† As the hydrogen evolution site, the existence of Rh metal is the key to determining the hydrogen evolution capacity. The hydrogen evolution rate of Step-STO-SSR loaded with Rh metal is 7.3 times higher than that of 18-STO-HM, because there are few effective hydrogen evolution sites in 18-STO-HM due to the absence of Rh metal. On the other hand, it is very difficult to improve the hydrogen evolution ability of the two kinds of STO only by loading chromium oxide or cobalt oxide. However, the photocatalysts loaded with Rh and subsequently with chromium/cobalt oxide *via* two-step photodeposition can improve the water-splitting activity to a certain extent, and the hydrogen evolution of Step-STO-SSR is increased to 1.3 times by loading chromium oxide and only 1.1 times by loading cobalt oxide.

Furthermore, the stability test of hydrogen production during the overall water splitting of Step-STO-SSR was carried out (Fig. S5b†), and the XRD and XPS characterizations over 8 h and 4 cycles are shown in Fig. 4a–d. The result shows that the structure of $SrTiO_3$ remained unchanged after the stability test, and the Rh metal and Cr_2O_3 as cocatalysts still exist, while cobalt oxide and rhodium oxide are partially decomposed. However, the synthetic $SrTiO_3$ photocatalyst is remarkably stable during the photocatalytic water-splitting reaction, reflected in the hydrogen production rate still maintaining a certain level, which proves that Rh metal and Cr_2O_3 play a certain role in hydrogen production.

The difference in the photocatalytic performances between the two kinds of strontium titanate is speculated to be mainly caused by the crystal face effect and vacancy effect. Based on the composition analysis of the step-shaped facet mentioned above, three kinds of STO crystal facets were simulated, which are the (100) crystal facet, (110) crystal facet, and Sr-rich (110) crystal facet, which are referred to as STO-(100), STO-(110), and STO-(110)_Sr respectively. DFT calculations were used to calculate the material work functions, which were determined by the material-specific electronic band structures, and besides the bulk electronic structure, surface properties also significantly influence the work function. The work function degree indicates the direction and possibility of electron transfer, lower the value, easier it is for electrons to leave the material.[40] Due to the advantages of chromium oxide in deposition and hydrogen production, we investigated the work function of the interaction between CrO_4^{2-} and $SrTiO_3$ crystal facets and further revealed the interaction mechanism and electron transfer between STO and chromate with different crystal facets and defects. More importantly, the photoelectric conversion ability of the crystal facet and vacancy to $SrTiO_3$ was evaluated using the $SrTiO_3$ and CrO_4^{2-} systems. Firstly, the work functions of the three kinds of facets are shown in Fig. 7a–c. The (100) crystal facet had a work function of 3.601 eV, while that of the (110) crystal facet was 4.81 eV, and that of the Sr-rich (110) crystal facet drops to 3.043 eV, proving that the (100) and Sr-rich (110) crystal facets are more prone to losing electrons. Therefore, it can be concluded that the Step-STO-SSR has more advantages in depositing cocatalysts and can effectively facilitate electron transfer. Next, the work functions of CrO_4^{2-} and $SrTiO_3$ crystal facets co-existing were calculated based on dipole correction as shown in Fig. 7d–f, abbreviated as STO-(100)-CrO_4^{2-}, STO-(110)-CrO_4^{2-}, and STO-(110)_Sr–CrO_4^{2-}. The results show that the work functions of the three different STO crystal facet systems have decreased obviously, which confirms the feasibility of electron transfer from the STO crystal facets to CrO_4^{2-}.

Furthermore, the electron density difference (EDD) was used to present the charge distribution and the direction of charge transfer to investigate the strength of charge transfer as shown in Fig. 7g and h. The blue area represents charge consumption, while the red area represents charge accumulation. There was a strong electron exchange between STO-(100) and CrO_4^{2-}, especially at the junction between the surface of strontium titanate and the bottom of chromate. According to the outcome, it is inferred that the photogenerated electrons of strontium titanate will be derived from the (100) crystal facet and transferred to chromate, resulting in the reduction reaction of chromate, which is consistent with the previous research results,[26] and the previous XPS analysis can confirm the valence change of chromate. However, the electron transfer between the STO-(110) facet and chromate was weaker than that between STO-(100) facet and chromate. Although there is a possibility of electron loss when the 110 plane coexists with chromate from the point of view of work function, the phenomenon of electron consumption on the (110) crystal facet occurs only on individual Ti atoms, and the chromate group has no obvious electron gain. Predictably, it is well known that $SrTiO_3$ has the characteristics of electron–hole anisotropy,[8] and the (110) crystal facet is a hole aggregation plane, leading to the poor ability to lose electrons, so there is almost no electron transfer behavior between the (110) crystal facet and chromate. In addition, there is weak charge transfer between Cr and O of chromate, meaning that if the redox reaction occurs in chromate on the STO-(110) facet, it is likely to be the charge transfer of Cr and O itself, rather than the photoelectron transfer on the $SrTiO_3$ surface, whereas, as

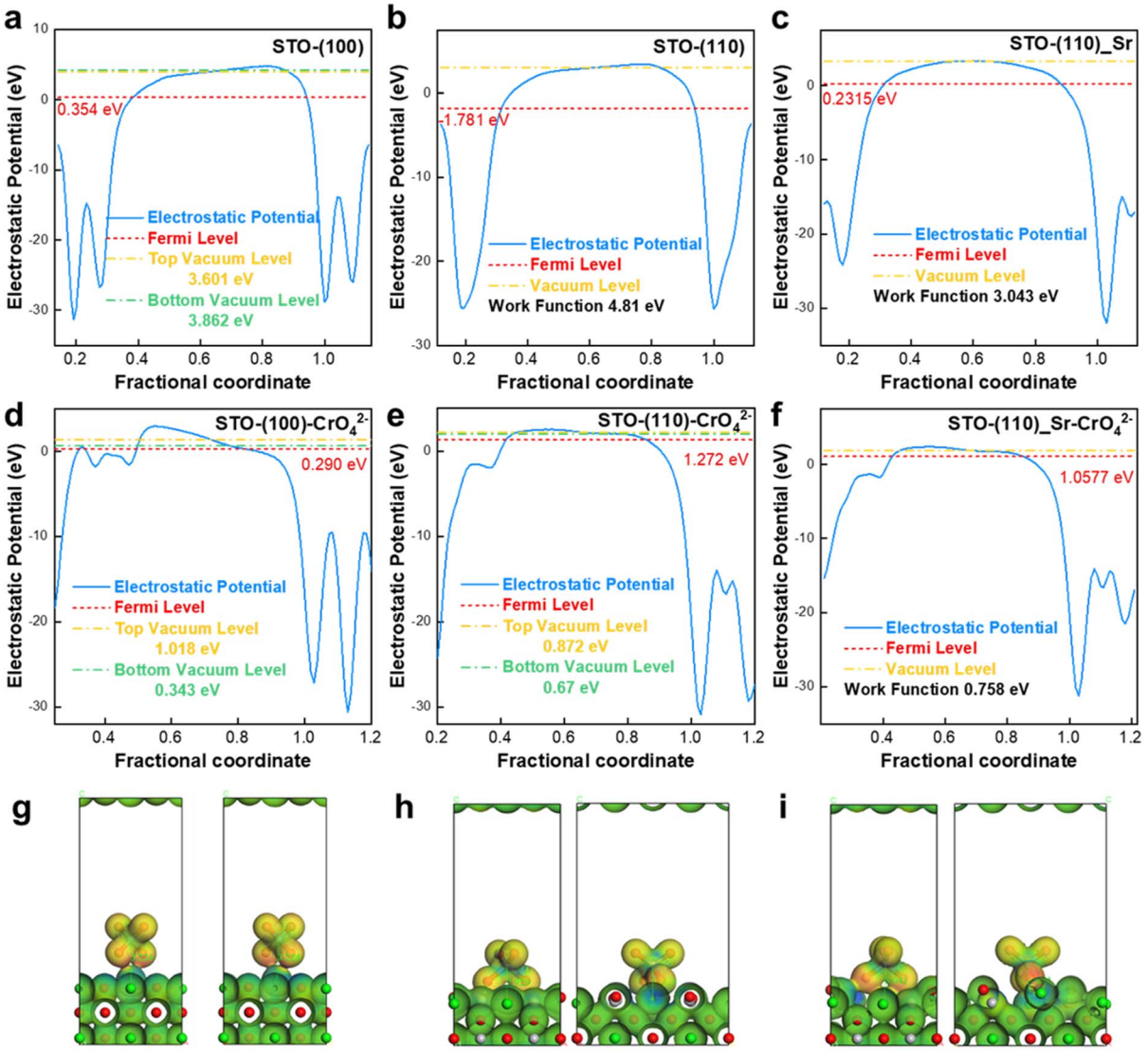

Fig. 7 The work function of STO-(100) (a), STO-(110) (b), STO-(110)_Sr (c), STO-(100)-CrO_4^{2-} (d), STO-(110)-CrO_4^{2-} (e), and STO-(110)_Sr–CrO_4^{2-} (f), respectively. EDD image for CrO_4^{2-} on STO (100) facet (g), STO (110) facet (h), and STO Sr-rich (110) facet (i).

speculated above, when the (110) crystal facet has the characteristics of being Sr-rich, anoxia, and titanium deficiency, the photooxidation property will be changed to photoreduction, resulting in electron loss. From the electron differential density of STO-(110)-CrO_4^{2-} and STO-(110)_Sr–CrO_4^{2-} based on the same color map range, the electron transfer between CrO_4^{2-} and Sr-rich interface is more obvious. The results show that the Sr-rich region of the (110) facet has higher reducibility, and is ready to lose electrons and thus transfer an electron to chromate.

These results clearly state that the crystal facet and vacancy effect affect the electronic activity of $SrTiO_3$, including the ability of electron overflow and effective electron transfer. Secondly, it confirms that the Step-STO-SSR with more (100) crystal facets and Sr-rich (110) crystal facets have advantages in photocatalytic activity, and provide guidance for subsequent research work. However, in our preliminary simulation work, the electron transfer between strontium titanate and trivalent rhodium has not yet been explored and will be followed up in subsequent studies.

4. Conclusions

A novel $SrTiO_3$ particle with the nano step-shaped crystal facet was prepared by the solid-state method based on hydrothermal octadecahedron $SrTiO_3$, and the mechanism of crystal facet formation was analyzed. Then, the composition of the crystal facet was characterized by thermal stability investigations and *in situ* XRD, resulting in the step-shaped crystal facet having O vacancy and Ti defect, forming a Sr-rich crystal surface, which is also confirmed by XPS and EPR techniques. In addition, the unique composition of the crystal facets changed the photo redox properties of $SrTiO_3$, with better bonding with Rh, Cr, and Co. The cocatalyst-loaded nano step-shaped crystal facet $SrTiO_3$

has a band gap shortened to 1.92 eV and longer carrier lifetime (3.736 ns), and its photocatalytic performance was measured in terms of the ability of photolytic overall water-splitting. The results show that the effective combination of the nano step-shaped crystal facet $SrTiO_3$ and cocatalysts makes it reach a higher hydrogen production rate, which is 4.6 times higher than that of the original octadecahedron $SrTiO_3$. Then, the influence of the $SrTiO_3$ crystal facet and vacancy on the photocatalytic capacity was analyzed by DFT, and the interaction between $SrTiO_3$ and chromate was taken as an example to conclude that the (100) crystal facet and Sr-rich (110) crystal facet were more effective in electron transfer, and the electron transfer between $SrTiO_3$ and CrO_4^{2-} was more obvious. Thence, the nano step-shaped crystal facet $SrTiO_3$ can achieve better photocatalytic activity, contributing to further improvement in the performance of overall water splitting.

Conflicts of interest

There are no conflicts to declare.

Acknowledgements

This work was funded by the Institute of Process Engineering, Chinese Academy of Sciences-NEWMAT (Beijing) Environmental Materials Technology Co., Ltd-Joint Laboratory of Photoelectronic New Materials Technology. We also appreciate the computation platform provided by Dr Gangqiang Yu of Faculty of Environment and Life of Beijing University of Technology.

Notes and references

1 L. Pan, H. Mei, G. Zhu, S. Li, X. Xie, S. Gong, H. Liu, Z. Jin, J. Gao, L. Cheng and L. Zhang, *J. Colloid Interface Sci.*, 2022, **611**, 137–148.
2 I. Tamiolakis, D. Liu, F. X. Xiao, J. Xie, L. T. Papadas, T. Salim, B. Liu, Q. Zhang, S. A. Choulis and G. S. Armatas, *Appl. Catal., B*, 2018, **236**, 338–347.
3 L. Mu, Y. Zhao, A. Li, S. Wang, Z. Wang, J. Yang, Y. Wang, T. Liu, R. Chen, J. Zhu, F. Fan, R. Li and C. Li, *Energy Environ. Sci.*, 2016, **9**, 2463–2469.
4 X. Yang, J. Cui, X. Liu, Q. Zhang, D. Wang, J. Ye and L. Liu, *Appl. Catal., B*, 2023, **325**, 122369.
5 M. N. Ha, F. Zhu, Z. Liu, L. Wang, L. Liu, G. Lu and Z. Zhao, *RSC Adv.*, 2016, **6**, 21111–21118.
6 L. Dong, H. Shi, K. Cheng, Q. Wang, W. Weng and W. Han, *Nano Res.*, 2014, **7**, 1311–1318.
7 P.-L. Hsieh, G. Naresh, Y.-S. Huang, C.-W. Tsao, Y.-J. Hsu, L.-J. Chen and M. H. Huang, *J. Phys. Chem. C*, 2019, **123**, 13664–13671.
8 T. Takata, J. Jiang, Y. Sakata, M. Nakabayashi, N. Shibata, V. Nandal, K. Seki, T. Hisatomi and K. Domen, *Nature*, 2020, **581**, 411–414.
9 Q. Jia, C. Wang, J. Liu, X. Cai, L. Zhong, G. Yu and D. Duan, *Nanoscale*, 2022, **14**, 12875–12884.
10 Q. Jia, C. Wang, J. Liu, X. Cai, L. Zhong, S. Chen, T. Li, G. Yu, L.-z. Wu and D. Duan, *Small*, 2022, **18**, 2202659.
11 Q. Jia, J. Liu, L. Zhong, Y. Li and D. Duan, *Mater. Lett.*, 2021, **288**, 129338.
12 C. Wang, J. Liu, X. Cai, Q. Jia and D. Duan, *J. Phys. Chem. C*, 2022, **126**, 15962–15970.
13 J. Ding, J. Bao, S. Sun, Z. Luo and C. Gao, *J. Comb. Chem.*, 2009, **11**, 523–526.
14 Z. Huang, Ariando, X. Renshaw Wang, A. Rusydi, J. Chen, H. Yang and T. Venkatesan, *Adv. Mater.*, 2018, **30**, 1802439.
15 R. A. Maier, A. C. Johnston-Peck and M. P. Donohue, *Adv. Funct. Mater.*, 2016, **26**, 8325–8333.
16 A. Tkach, O. Okhay, A. Almeida and P. M. Vilarinho, *Acta Mater.*, 2017, **130**, 249–260.
17 S.-M. Wu, X.-L. Liu, X.-L. Lian, G. Tian, C. Janiak, Y.-X. Zhang, Y. Lu, H.-Z. Yu, J. Hu, H. Wei, H. Zhao, G.-G. Chang, G. Van Tendeloo, L.-Y. Wang, X.-Y. Yang and B.-L. Su, *Adv. Mater.*, 2018, **30**, 1802173.
18 K. Wu, J. Xiong, Y. Sun, J. Wu, M. Fu and D. Ye, *J. Hazard. Mater.*, 2022, **428**, 128172.
19 Y. A. Abramov, V. G. Tsirelson, V. E. Zavodnik, S. A. Ivanov and I. D. Brown, *Acta Crystallogr.*, 1995, **51**, 942–951.
20 X. H. Zhu, J. M. Zhu, S. H. Zhou, Z. G. Liu, N. B. Ming and D. Hesse, *J. Cryst. Growth*, 2005, **283**, 553–562.
21 X. H. Zhu, J. Zhou, J. M. Zhu, Z. G. Liu, Y. Y. Li and T. Al-Kassab, *J. Am. Ceram. Soc.*, 2014, **97**, 1987–1992.
22 P. Hartman and W. G. Perdok, *Acta Crystallogr.*, 1955, **8**, 49–52.
23 W. Xu, P. C. Bowes, E. D. Grimley, D. L. Irving and J. M. LeBeau, *Appl. Phys. Lett.*, 2016, **109**, 201601.
24 V. P. Pakharukova, D. I. Potemkin, O. A. Stonkus, N. A. Kharchenko, A. A. Saraev and A. M. Gorlova, *J. Phys. Chem. C*, 2021, **125**, 20538–20550.
25 A. R. Mazza, Q. Y. Lu, G. X. Hu, H. X. Li, J. F. Browning, T. R. Charlton, M. Brahlek, P. Ganesh, T. Z. Ward, H. N. Lee and G. Eres, *ACS Appl. Mater. Interfaces*, 2022, **14**, 10898–10906.
26 Z. Y. Su, F. Fang, X. Li, W. J. Han, X. L. Liu and K. Chang, *J. Colloid Interface Sci.*, 2022, **626**, 662–673.
27 M. Shah, Y. Z. Lu, N. Mushtaq, M. Yousaf, S. Rauf, M. I. Asghar, P. D. Lund and B. Zhu, *Sustainable Energy Fuels*, 2022, **6**, 3794–3805.
28 H. Q. Tan, Z. Zhao, W. B. Zhu, E. N. Coker, B. S. Li, M. Zheng, W. X. Yu, H. Y. Fan and Z. C. Sun, *ACS Appl. Mater. Interfaces*, 2014, **6**, 19184–19190.
29 R. Lin, J. Wan, Y. Xiong, K. Wu, W. C. Cheong, G. Zhou, D. Wang, Q. Peng, C. Chen and Y. Li, *J. Am. Chem. Soc.*, 2018, **140**, 9078–9082.
30 N. Liu, M. Xu, Y. Yang, S. Zhang, J. Zhang, W. Wang, L. Zheng, S. Hong and M. Wei, *ACS Catal.*, 2019, **9**, 2707–2717.
31 W. G. Pan, M. H. Cao, C. L. Diao, C. Tao, H. Hao, Z. H. Yao, Z. Y. Yu and H. X. Liu, *J. Mater. Sci.*, 2019, **54**, 12401–12410.
32 Y. Zhu, P. A. Salvador and G. S. Rohrer, *ACS Appl. Mater. Interfaces*, 2017, **9**, 7843–7851.
33 A. S. Pisat, P. A. Salvador and G. S. Rohrer, *Adv. Mater. Interfaces*, 2019, **6**, 1900731.

34 X. Huang, H. Liu, S. Zhang, G. Li, H. Hao, M. Cao, Z. Yao and J. Xie, *J. Mater. Sci.: Mater. Electron.*, 2018, **29**, 11546–11552.
35 Z. Chen, X. P. Shan, G. Y. Li, N. Huang, H. Hao and H. X. Liu, *J. Mater. Sci.: Mater. Electron.*, 2016, **27**, 10627–10633.
36 F. Polo-Garzon, Z. Bao, X. Zhang, W. Huang and Z. Wu, *ACS Catal.*, 2019, **9**, 5692–5707.
37 A. Cakra Wardhana, A. Yamaguchi, S. Shoji, M. Liu, T. Fujita, T. Hitosugi and M. Miyauchi, *Appl. Catal., B*, 2020, **270**, 118883.
38 S. A. Khan, S. B. Khan and A. M. Asiri, *New J. Chem.*, 2015, **39**, 5561–5569.
39 Z. Wang, C. Li and K. Domen, *Chem. Soc. Rev.*, 2019, **48**, 2109–2125.
40 D. Chen, R. Lu, R. Yu, Y. Dai, H. Zhao, D. Wu, P. Wang, J. Zhu, Z. Pu, L. Chen, J. Yu and S. Mu, *Angew. Chem., Int. Ed.*, 2022, **61**, e202208642; *Angew. Chem.*, 2022, **134**, e202208642.